Venus Entry Flow over a Decomposing Aeroshell in X2 Expansion Tube

Nikhil Banerji* and Pénélope Leyland†
Ecole Polytechnique Fédérale de Lausanne, 1015 Lausanne, Switzerland
and
Elise Fahy‡ and Richard Morgan§
University of Queensland, St. Lucia, Queensland 4072, Australia

DOI: 10.2514/1.T5172

The effects of phenolic decomposition on shock-layer radiation were investigated experimentally in X2 expansion tube for a Venus entry flow. A carbon–phenolic composite aeroshell was subjected to a flow with a flight equivalent velocity of 9.35 km · s^{-1}. Emission spectroscopy was used to measure boundary-layer radiation in parts of the ultraviolet (380–480 nm) and visible (620–700 nm) spectrum, and it was compared to control measurements taken with a cold steel model. With the composite model in place, the calibrated spectral radiance measured was seen to increase for the O (645.598 nm) atomic line and the N_2^+ (391.22 nm) band head, but it decreased for the C_2 Swan band (420–480 nm). The recorded data were then compared to numerical spectra produced by two-dimensional axisymmetric computational fluid dynamic simulations coupled to a radiation solver. Both of the applied chemistry models overpredicted CN violet $\Delta\nu = 0$ band radiation, which demonstrated strong self-absorption at these conditions. Better comparisons were achieved for the C_2 Swan band radiation. At visible wavelengths, peak intensities were underestimated by the numerical simulations. Several possible reasons were hypothesized for these discrepancies.

Nomenclature

A	=	area of the cell boundary per unit radian in the circumferential direction, m^2
E_a	=	activation energy, kJ · mol^{-1}
$\bar{F}_i$	=	inviscid flux vector
$\bar{F}_v$	=	viscous flux vector
$\hat{n}$	=	outward-facing normal of control surface
p	=	pressure, Pa
Q	=	source term
T	=	temperature, K
u	=	velocity, m · s^{-1}
V	=	volume, m^3
X	=	mass fractions
α	=	thermal diffusivity, m^2·s^{-1}
Γ	=	Goulard number
γ_i	=	efficiency of reaction i
∂v	=	bounding surface
ϵ	=	emission coefficient, W · m^{-3}
κ	=	absorption coefficient, m^{-1}
ρ	=	density, kg · m^{-3}

Subscripts

ν	=	frequency
∞	=	freestream

Presented as Paper 2016-3231 at the 46th AIAA Thermophysics Conference, Washington, D.C., 13–17 June 2016; received 9 January 2017; revision received 26 June 2017; accepted for publication 22 July 2017; published online 31 August 2017.

*Ph.D. Student, Station 9, Interdisciplinary Aerodynamics Group. Student Member AIAA.
†Group Leader, Station 9, Interdisciplinary Aerodynamics Group. Member AIAA.
‡Ph.D. Student, Centre for Hypersonics. Student Member AIAA.
§Director, Centre for Hypersonics. Associate Fellow AIAA.

I. Introduction

THERMAL protection systems (TPSs) are employed in spacecraft heat shields to survive extreme thermal loads in high-enthalpy conditions. In an attempt to reduce structural and fuel loads, and simultaneously increase payload capacity, modern composite porous materials such as low-density carbon–phenolics are being investigated [1]. The ablation and pyrolysis of these materials affect the surrounding flow structure, and hence the radiation, both of which significantly modify the heat transferred to the vehicle wall. Given the cost and rarity associated with flight tests, the response of these modern materials in extreme environments is best investigated using a combination of ground tests and numerical simulations.

These materials are often tested in arcjets [2]. These facilities can reproduce realistic heating rates with test times sufficient to achieve thermal equilibrium via aerothermal heating. However, they lack the ability to sufficiently recreate the nonequilibrium hypersonic flow surrounding an entry vehicle and its response to ablation. They are therefore used primarily for material characterization [3]. Alternatively, hypersonic impulse facilities, which produce shock-layer radiation similar to flight, are used to test-scaled models of entry vehicles [4]. The effects of ablation on air shock layers have been the subject of several previous test campaigns in X2 expansion tube at the University of Queensland in Australia. Buttsworth et al. [5] tested scaled stainless-steel models of the Hayabusa capsule that were layered with an epoxy resin. Upon encountering the hot hypersonic flow, the resin started to pyrolyze. This effect was visualized through the presence of CN in boundary-layer radiation measurements. The Achilles' heel of impulse facilities is their inability to sustain the flow for long enough to accurately reproduce ablation and pyrolysis. In an attempt to eliminate the initial time requirement, Zander et al. [6] developed a resistive heating technique to electrically heat a flat-faced model of a cylindrical section of reinforced carbon–carbon to approximately 2300 K before flow establishment, showing an increased production of CN due to wall temperature. Lewis et al. [7] investigated CN violet emissions at a range of different wall temperatures for the same model.

Computational fluid dynamic (CFD) simulations have been used to numerically rebuild several expansion tube experiments [8]. Potter used two-dimensional (2-D) axisymmetric CFD coupled to the in-house radiation code `Photaura` to compare shock-layer radiation, simulated around a cylindrical model in a Martian flow, to

experiments [9]. Similarly, Fahy et al. [10] rebuilt the flow around a scaled model of the Hayabusa capsule and compared the simulated radiation from its shock layer to experiments and to flight. Palmer et al. [11] conducted a similar study for Mars and Titan gas mixtures. Alba et al. [12] simulated radiation measurements obtained from the aforementioned experiments by Lewis et al. [7], coupling a three-dimensional (3-D) CFD solution to the radiation code NEQAIR, Version 13.2.

Due to the operating envelope of existing ground test facilities, a lack of accurate experimental data is even more severe for nonterrestrial entry conditions. Venus's hot, dense atmosphere will prove a stern test for any entry vehicle, therefore making a better understanding of its entry environment crucial for future missions. Experiments conducted during this work therefore build on previous investigations by looking at the effect of species produced at the surface of a decomposing carbon–phenolic model in a Venusian aerocapture-type entry condition [2,13,14]. This work will also expand on the previous simulations by including the coupled effects of ablation and radiation on the highly nonequilibrium, axisymmetric Venusian flow surrounding the phenolic aeroshell model.

II. Experimental Methodology

The University of Queensland's X2 facility (Fig. 1) is a free piston-driven expansion tube that is configured with a freely sliding piston, a shock tube containing the test gas, an acceleration tube, and a nozzle exiting into a test section where the model is mounted. Its operation has been described in detail by Gildfind et al. [8], and thus will only be briefly summarized here.

The tube was sealed with the shock tube separated from adjacent sections by the primary and secondary diaphragms, made of mild steel and aluminum foil, respectively. Each section was evacuated, and the optical system was aligned with the model surface. For this work, the acceleration tube and test section were then held at a pressure of 40 Pa, whereas the shock tube was filled with 3.6 kPa of the Venus-like 96% CO_2–4% N_2 test gas. When using a 2-mm-thick primary diaphragm, 6.85 MPa of air was pumped in behind the piston, and the condition-specific driver gas (helium, in the case of these experiments) was added at 92.8 kPa. Both radiation and pressure measurements were triggered using a photodiode aimed at the nozzle exit and combined with a trigger connected to a data box. Once triggered (Fig. 2), a delay of 40 μs was allowed for the flow to steady.

A. Condition Selection and Testing

A Venus shot condition, designed by de Crombrugghe de Looringhe [14], was adopted for these experiments. Table 1 provides the freestream conditions estimated using Pitot [15], which is an equilibrium expansion tube and shock tunnel analysis code that uses the tube configuration parameters and measured shock velocities as an input to calculate these properties.

Experimental shock speeds were calculated using a range of pressure transducers mounted on the tube walls. Test flow conditions were estimated, before the main experiments, from nine 15-deg cone heads in a vertical rake spaced at 18 mm and positioned just downstream of the nozzle exit plane. This also allowed an estimation of a core flow diameter and steady test time, which was estimated as $t \sim 70$ μs from Fig. 2. Pitot transducers 3 to 9 collected similar data, giving a core flow diameter of approximately 108 mm, which was then the limiting factor for the diameter during model design.

B. Model Development and Bench Testing

A fiberglass-reinforced phenolic sphere–cone was cast with a nose radius of 19.5 mm, a diameter of 60 mm, and a sphere–cone angle of 60 deg. The chosen aeroshell shape deviated from previous ablation studies in X2, which used semi-hemispherical models. The design was intended for use with multiple entry conditions and gas compositions in X2. It was therefore not a scaled-down geometry of a specific, flown entry vehicle. The experiments were also designed

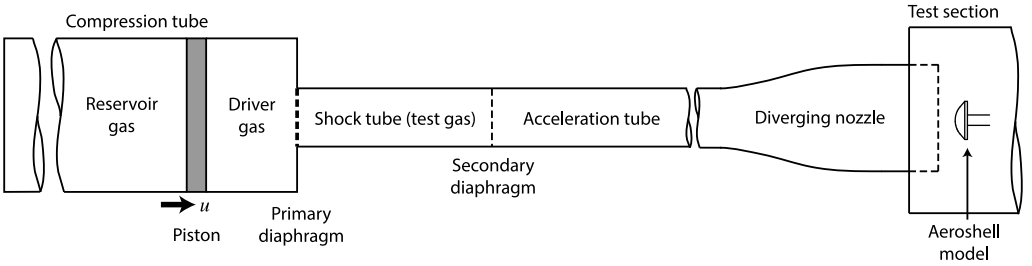

Fig. 1 Schematic diagram of X2 [4] (not to scale).

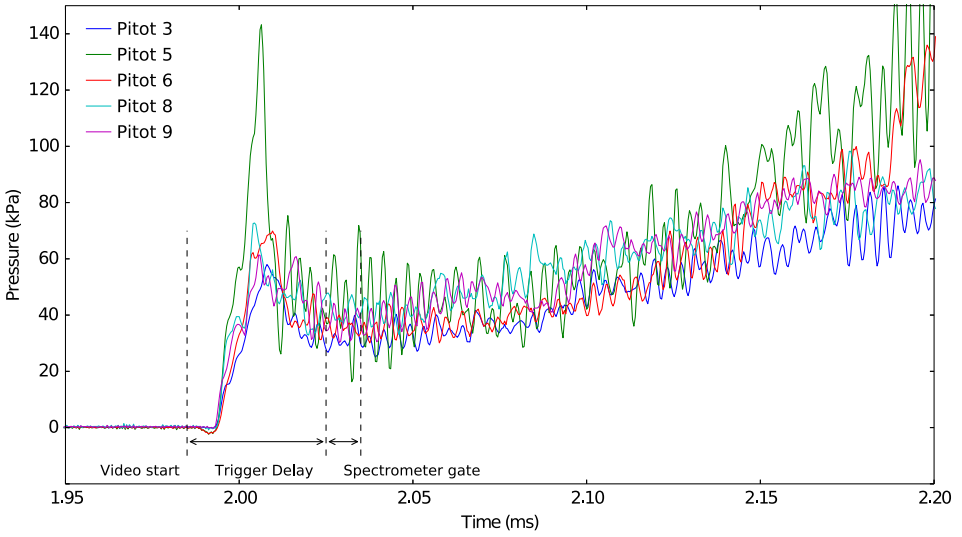

Fig. 2 Pitot traces for Venus condition test shot X2s2488. Raw data from de Crombrugghe de Looringhe [14].

Table 1 Estimated freestream X2 conditions for Venus entry

Parameter	Value
T_∞, K	2780.91
p_∞, Pa	4064.0
ρ_∞, kg · m^{-3}	5.1×10^{-3}
u_∞, m · s^{-1}	9347.2
X_{CO_2}	0.2622
X_{CO}	0.4433
X_{N_2}	0.0193
X_{NO}	0.005
X_{O_2}	0.168
X_O	0.1023

with ease of numerical rebuilding in mind, facilitated by the axisymmetry of the aeroshell shape and two-dimensional behavior of the surrounding flow.

Due to its low thermal conductivity, the use of the fiberglass shell ensured the preservation of model structural integrity, allowing for reusability. Approximately 25% by weight fiberglass content was used. Sixteen plies were laid up in a $[0/90]_{4s}$ cross-plied configuration, and the model was cured for 60 min at 60°C. The model was then removed from the mold and cured again for 240 min at 80°C. A layer of Cellobond Resin J2027L [16], comprised of 7–10% phenol and 2–3% formaldehyde and water, mixed with chopped Torayca T700S carbon fibers [17] was applied to the flow-facing surface. The model was once again cured for 240 min at 80°C. The final model is shown in Fig. 3.

Due to the brittleness of the phenolic resin, electrical preheating of the model was abandoned in favor of shock heating, which was similar to Buttsworth et al. [5], i.e., the hot flow increased the surface temperature and caused the model to decompose. The thermal diffusivity of a typical carbon–phenolic TPS is $\alpha \sim 10^{-6}$ m^2 · s^{-1} [18], giving a penetration distance of approximately $\sqrt{8\alpha t_{\text{test}}} \sim 24$ μm for a steady test time of $t_{\text{test}} \sim 70$ μs. It is therefore reasonable to estimate the rise in surface temperature using a one-dimensional semi-infinite approximation,

$$\Delta T_{\text{test}} = \frac{2q}{\pi\sqrt{\rho c k}} t_{\text{test}} \tag{1}$$

Using Sutton and Graves's empirical correlation [19] for stagnation-point heat transfer in CO_2–N_2 atmospheres, the heat flux incident on the model is estimated as 7900 W · cm^{-2} for the flow condition. This value is of the same order as the CFD calculated incident heat flux, detailed in Sec. IV.B. Taking thermal effusivity as $\sqrt{\rho c k} \sim 2200$ kg · s$^{-5/2}$ · K^{-1} [18], a temperature rise of between 300 and 350 K is estimated, resulting in a wall temperature of approximately 600 K, and causing the onset of resin decomposition [20].

C. Optical Setup

Once the condition was tested and the model mounted in the X2 test section, the optical systems were set up and the tests were performed. The aim of these experiments was to measure emission from the phenolic products added to the flow through outgassing or surface reactions. The experiments concentrated specifically on measuring increased emission from C and O in the visible range (615–700 nm) and CN violet and C_2 Swan bands in the ultraviolet (UV) range (380–480 nm). Figure 4 illustrates the layout of the optical setup, with the ultraviolet spectrometer to the left of the tunnel and the high-speed camera and infrared spectrometer to its right. The infrared system on the right of the tube has been omitted in the schematic for clarity. Visible radiation from the ablation layer was measured through a Perspex® window for a narrow horizontal strip parallel to and including the stagnation streamline. Ultraviolet radiation was similarly measured through a fused silica window.

A magnification of 2:1 was achieved by focusing the radiation using a concave spherical mirror with a focal length of 500 mm. An aluminum turning mirror and a periscope were then used to rotate the image by 90 deg onto the vertical spectrometer slit. The captured light was spectrally resolved with an Acton Research Spectro Pro 2300I spectrograph using a 600 lines/nm diffraction grating coupled to a Princeton Instruments PI-MAX intensified charge-coupled device (ICCD) camera. The settings for both spectrometers are provided in Table 2. A Shimadzu HPV-1 high-speed camera was also positioned on a raised mount and imaged the model via a flat aluminum turning mirror placed above the test section. A delay of 40 μs was used to try and avoid the flow establishment period before the shock layer became steady (as shown in Fig. 2).

The ICCD detector recorded a signal in counts related to the radiation emitted from the shock layer. This signal was converted to spectral radiance via intensity calibration, which takes into account sensitivity of the detector, collection efficiency of the optics, and losses due to optical components. A Labsphere CSTM-LR-2Z-4 Integrating sphere with a known spectral radiance was placed in the position of the model, accounting for all of the components along the optical path in the recorded image. From this image and the known spectral radiance profile of the source, a pixel-by-pixel calibration matrix was used to quantify the raw data. Background counts occurred due to thermal noise, even though the ICCD was cooled to 253 K during all experiments. These were therefore recorded from the regions on the ICCD not exposed to incoming light, and they were subtracted from the images during postprocessing. Cosmic rays occasionally caused bright spots on the ICCD, but these were also removed during post-processing. Wavelength calibration was performed using a light source with two known spectral lines, such as a fluorescent lamp.

III. Numerical Methodology

As shown in previous studies [9,10,12], spectra recorded from experiments in X2 can be numerically rebuilt, within the limits of

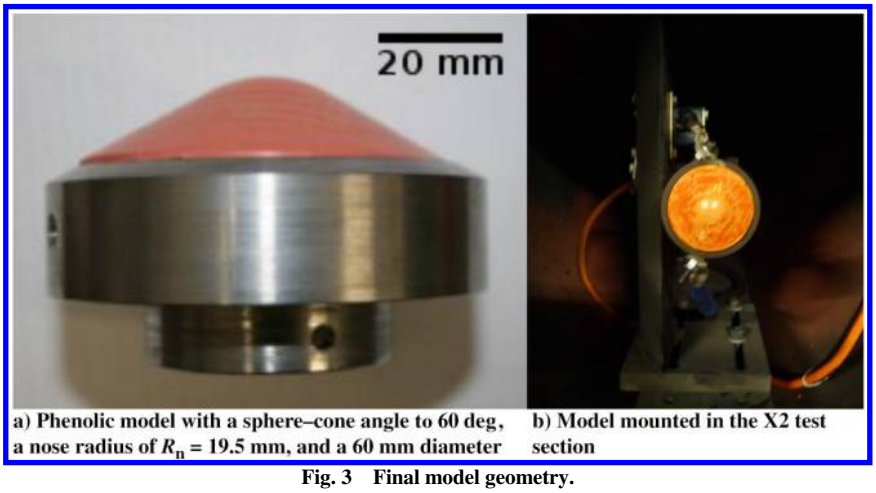

a) Phenolic model with a sphere–cone angle to 60 deg, a nose radius of R_n = 19.5 mm, and a 60 mm diameter

b) Model mounted in the X2 test section

Fig. 3 Final model geometry.

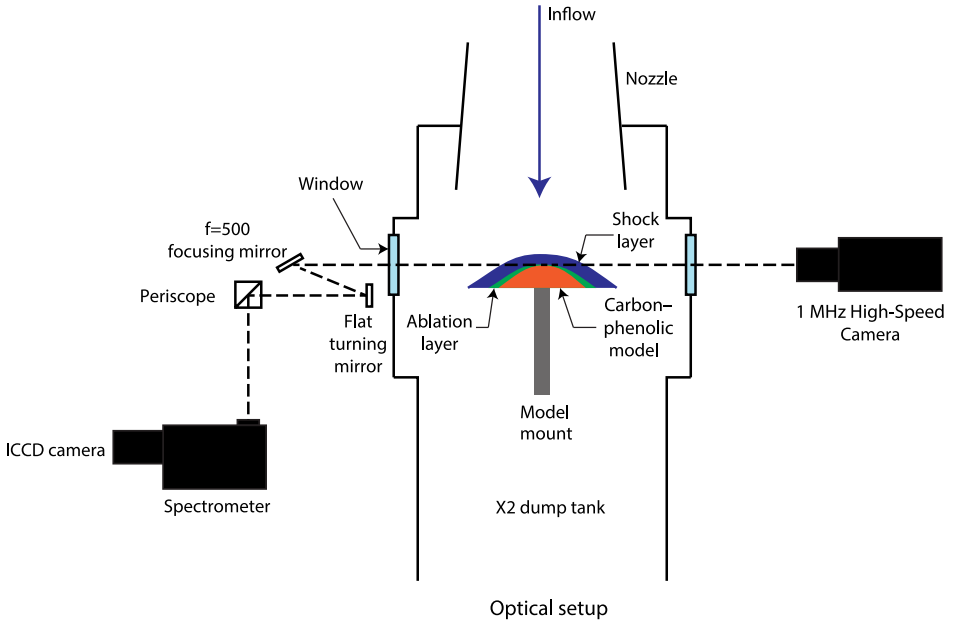

Fig. 4 Illustration of the optical setup used for ultraviolet and visible radiation measurements (adapted with permission from the work of Fahy et al. [10]).

uncertainties in selected freestream conditions, numerical methods, and experimental data. This was attempted for the aforementioned model in a Venusian atmosphere simulated in X2. CFD simulations were used to model the hypersonic, nonequilibrium flow surrounding the model. This solution was then coupled to a radiation code to calculate the line-of-sight spectra that were compared to the experimental spectrum.

A. Flowfield Modeling

`Eilmer3` is the compressible flow CFD code developed by the University of Queensland, with contributions from Ecole Polytechnique Fédérale de Lausanne and other research institutes. The solver uses a cell-centered, finite volume approach to the integral form of the compressible Navier–Stokes equations on 2-D or 3-D structured multiblock grids [21]. The time-resolved integration of the conserved quantities was conducted in the following form,

$$\frac{\partial}{\partial t}\int_V U\,\mathrm{d}V = -\oint_{\partial v}(\bar{F}_i - \bar{F}_v)\cdot\hat{n}\,\mathrm{d}A + \int_V Q\,\mathrm{d}V \tag{2}$$

The source terms Q are a combination of geometry (for axisymmetry), chemistry, thermal energy exchange, and radiation components. The conserved quantities U include overall and species densities, the momentum per volume in the x and y directions, as well as the energy per volume. The flux vectors are divided into inviscid and viscous contributions.

Due to the high enthalpy of the freestream, thermochemical nonequilibrium was expected in the shock layer, excluding the use of Park et al. [22] and Park and Ahn's [23] one-temperature assumption for CO_2–N_2 flows. A two-temperature model was thus used to simulate the thermal nonequilibrium, coupling translational–rotational and vibrational-electron–electronic modes. The Millikan–White model with the Park high-temperature correction was used for vibrational relaxation, whereas the Appleton–Bray ion or neutral models were applied for translation–electron energy exchange. Chemistry–vibration coupling was accounted for by Treanor and Marrone's [24] model. Park et al.'s Mars reaction model [22] was modified to contain 17 species and 43 reactions, omitting the inclusion of Ar because it was only present in trace amounts. A comparison was made with Johnston and Brandis's model [25], comprising 16 species and 34 reactions for CO_2–N_2 flows, which presented tuned kinetic rates to match CO fourth-positive and CN Violet band radiation measured at NASA's Electric Arc Shock Tube facility. The Gupta–Yos mixing rule [26,27] was applied, with the relevant collision integrals [28,29], to calculate the viscosity and thermal conductivity of the mixture. Ramshaw and Chang's [30] self-consistent effective binary diffusion approximation to the Stefan–Maxwell equations was used to calculate mass diffusion. Turbulence modeling was not included [9,10,12].

Table 2 Spectrometer settings

	Ultraviolet	Visible
Center wavelength, nm	440	656
Gain, dB	110	150
FWHM, Å	4.1	4.5
$\Delta\lambda$, nm/pixel	0.14	0.14
Δx, μm/pixel	26	26
Grating, lines/mm	600	600
Effective wavelength range, nm	80	80
Slit width, μm	50	50
Exposure time, μs	10	10
Trigger delay, μs	40	40

An axisymmetric structured grid was used for the simulations, including the model forebody and shoulder. The cells were clustered toward the wall and around the shock in the x direction to resolve the boundary layer and nonequilibrium region, respectively. The final simulation was conducted with 120×190 cells, weakly clustered toward the stagnation line in the y direction. A grid convergence study[¶] [31,32] was conducted using two coarser grids, with 50 and 25% of the cells in both the x and y directions, giving an overall refinement ratio of four. The shock-layer equilibrium temperature at zero-grid spacing was estimated to be $T = 10,198$ K with an error band of 0.148%, as shown in Fig. 5. The calculated order of convergence was 1.033 m which was suitably close to one and indicated that the solutions were in the asymptotic range of convergence for simulations involving a shock layer (see footnote ¶).

A fixed surface temperature of 600 K was used along with a noncatalytic wall to simulate the steel model. For the phenolic case, the implemented surface reaction boundary condition was limited to oxidation and nitridation of surface carbon, as per the equations and kinetic rates provided by Park et al. [33]. Reactions involving C_3 were excluded from the model, as its abundance did not become significant until surface temperatures reached 3000 K [34]. The required Arrhenius parameters are given in Table 3. The importance of nitridation to surface mass loss and radiative heating has resulted in

[¶]Slater, J.W., "Examining Spatial (Grid) Convergence," Public Tutorial on CFD Verification and Validation, Vol. 86, NASA John H. Glenn Research Center, Cleveland, OH.

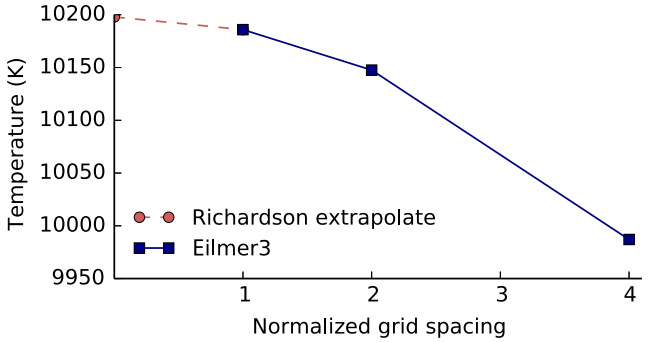

Fig. 5 Spatial convergence of mesh used for model simulations in `Eilmer3`.

several different models, which were summarized by Alba et al. [12]. The modification to the Park surface reaction model by Suzuki et al. [35] proposed a reduced efficiency of nitridation for lower temperatures, showing better agreement with efficiencies obtained experimentally. In this work, both surface kinetic models were considered.

B. Radiation Modeling

To compare to experimental data, numerical spectra were determined by solving the radiative transfer equation (RTE) given by the following,

$$I_\nu(s) = I_\nu(s_0)e^{-\kappa_\nu(s_0,s)} + \int_{s_0}^{s} \epsilon_\nu(s')e^{-\kappa_\nu(s',s)}\,\mathrm{d}s' \tag{3}$$

with scattering ignored in weakly ionized plasmas due to low gas density. The frequency-dependent intensity, I_ν, was solved for as a function of emission and absorption coefficients, ϵ_ν and κ_ν, and path length s.

A radiation code was then used to calculate the emission and absorption coefficients when supplied with flowfield properties at a discrete point. Quasi-steady-state nonequilibrium radiation involving collisional–radiative mechanisms was combined with equilibrium radiation determined by the Boltzmann distribution. The `Photaura` [9], `PARADE` (Version 3.2) [36], and `NEQAIR` (Version 14) [37] codes were used, with differences in the databases resulting in different calculated intensities. The result that best matched the experimental spectra is shown here, with comparisons of the codes themselves not within the scope of this work. A spectral resolution of 100 points/nm was used over a wavelength range from 380 to 500 nm in the ultraviolet and 615 to 700 nm in the visible. To rebuild the exact data recorded by the spectrometer, a line-of-sight calculation was conducted for selected coordinates in the flowfield, travelling through the shock layer until the stagnation line. The effects of broadening mechanisms on the physical flow were numerically reproduced as a Voigt profile with Gaussian and Lorentzian line widths equivalent to the experimentally obtained full width at half–maximum (FWHM), given in Table 2, for each instrument.

`Eilmer3` allows the inclusion of a radiative source term in the Navier–Stokes equations, if desired. The degree of radiation–flowfield coupling can be estimated via the Goulard number Γ, which is the conversion of the freestream energy flux to incident radiative energy flux. This is defined as follows,

$$\Gamma = \frac{2q_{\mathrm{rad}}}{(1/2)\rho_\infty u_\infty^3} \tag{4}$$

where q_{rad} is the incoming radiative heat flux and, ρ_∞ and u_∞ are the density and velocity of the freestream, respectively. As a rule of thumb, when $\Gamma > 0.01$, it generally indicates that the flow is strongly coupled [38]. For the condition being studied, stagnation-point radiative heat flux was calculated to be 3410 $\mathrm{W \cdot cm^{-2}}$ via a tangent slab approximation, based on stagnation line temperatures and species number densities calculated and described in Sec. IV.B. The Goulard number was thus equal to $\Gamma \sim 0.003$, which is below the aforementioned threshold. Inclusion of the radiative source term was therefore thought to have a negligible effect on the flowfield and was consequently excluded from this study.

IV. Results

A. Experimental Results

Still photographs taken by the Shimadzu HPV-1 high-speed camera demonstrate the start and end of the steady test time during the V1 flow condition, shown in Figs. 6a and 6c, respectively. The shock detachment distance can be estimated at approximately 1.9 mm through use of a Canny edge detection filter, as seen in Fig. 6b.

All spectra were extracted from radiation measurements taken at a distance of 0.1 mm from the phenolic and steel model surface, which were spatially averaged over ± 1 pixel, giving an averaged spatial resolution of 0.08 mm. Experimental UV spectra centered at 440 nm are presented in Fig. 7. In both spectra, CN violet and C_2 Swan bands are visible, as well as the N_2^+ band head. There are a number of peaks corresponding to Fe and Al contamination due to residue from the burst diaphragms. The spectra have been normalized by the maximum intensity of their highest peak to remove the effect of temperature differences caused by shot-to-shot variation.

It can be seen that the N_2^+ first-negative $\Delta\nu = 0$ band head gains in intensity, and CN violet intensity is unchanged; whereas the C_2 Swan bands lose intensity in the presence of the composite model. A similar phenomenon was noted by Eichmann [39], who suggested a reduced CO_2 concentration of the test gas as a reason for weak CN and C_2 band structure in Martian flows. A reduction in CO_2 would leave more unreacted N_2 in the flow to ionize. Given the high density and velocity of the Venusian flow investigated, along with the comparatively high test section pressure of 40 Pa (compared to 10 Pa used by Eichmann), this is certainly a possibility. However, given the stasis of CN violet band intensities between shots, C_2 dissociation could also be linked to creation of other carbon-based species after reaction with hydrocarbon components of the phenolic resin.

Normalized spectra recorded in the visible range, for the composite and cold steel models, are presented in Fig. 8. No change is observed for the CN red band and C atomic line spectra between the two datasets. However, an increase in atomic O emission is seen in the presence of the composite model. This increase could be due to an increased concentration of atomic O in the boundary layer due to reactions on the composite model surface.

B. Flowfield Results

Flowfield results for the aeroshell model in a simulated Venus entry flow in X2 are detailed in this section. The stagnation line profiles for translational–rotational T_{tr} and vibrational-electron–electronic T_{ve} temperatures using both Park (solid lines) and Johnston (dashed lines) models are presented in Fig. 9a. Using the Park model, a peak in T_{tr} of 44,300 K is calculated. Over a nonequilibrium region of approximately 1.08 mm, both thermal modes relax to an equilibrium temperature of 10,162 K. The equilibrium region then continues until the model wall. Modeling the gas chemistry using the Johnston model, a lower peak T_{tr} of approximately 39,726 K is observed. The two thermal modes

Table 3 Surface ablative reactions and Arrhenius rate parameters

	Reaction	γ_i	E_a, $\mathrm{kJ \cdot mol^{-1}}$	Reference
1)	$O + C(s) \rightarrow CO$	0.63	9.644	[33]
2a)	$N + C(s) \rightarrow CN$	0.30	0	[33]
2b)		$8.441 \times 10^{-3} \exp(-2322/T_w)$	0	[35]

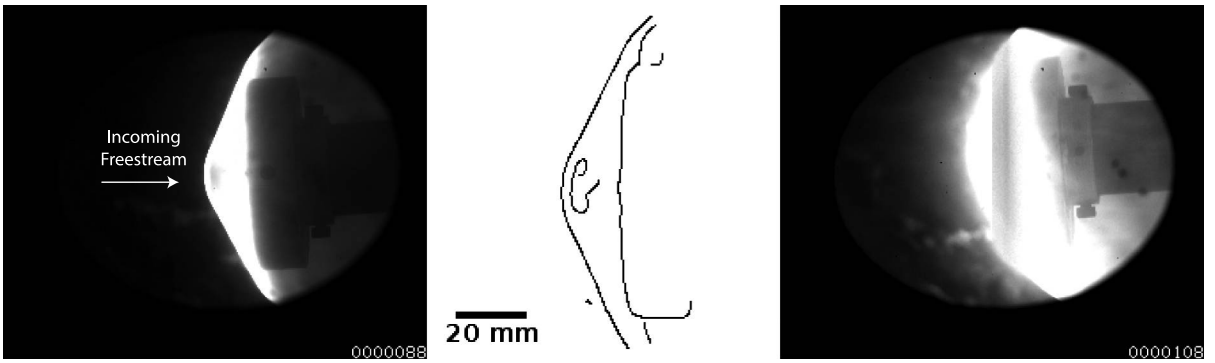

a) Steady test time

b) Canny edge detection result showing a shock detachment distance of 1.9 mm

c) End of steady test time

Fig. 6 Side-on views taken by HPV-1 camera during test flow.

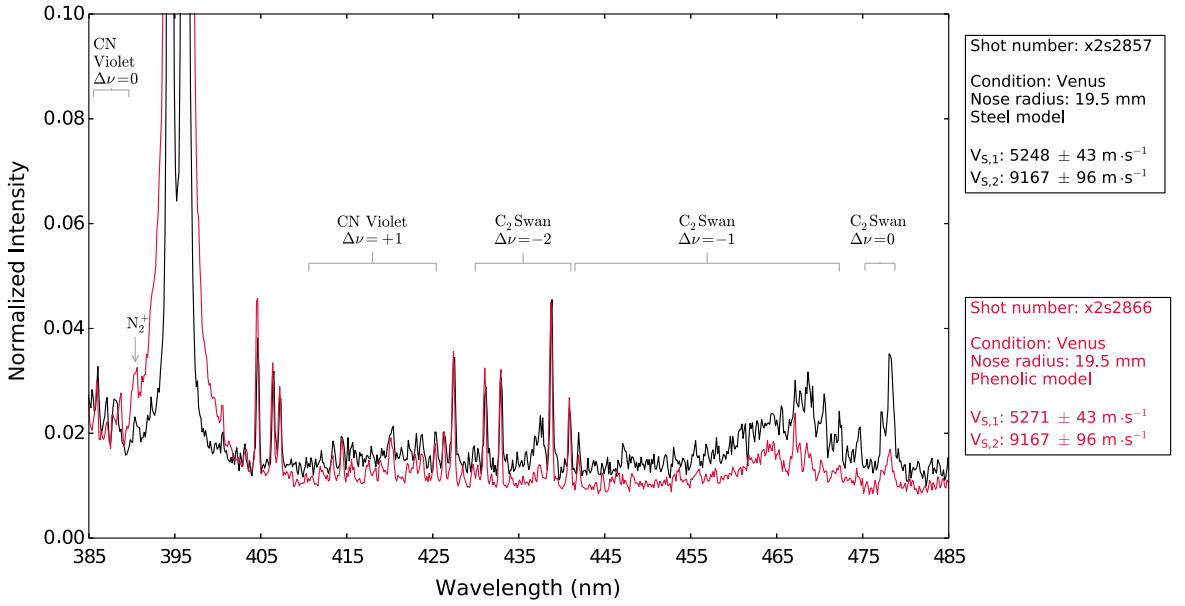

Fig. 7 Normalized spectra in the UV wavelength range, collected at a distance of 0.1 mm from the steel and phenolic model surfaces.

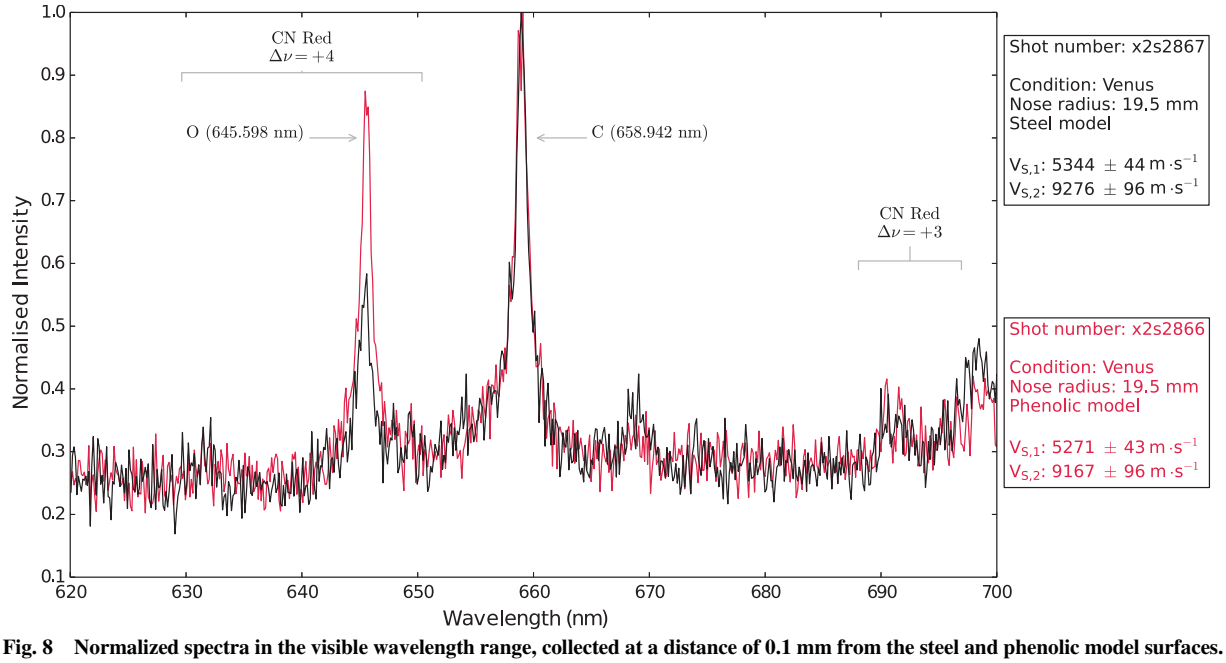

Fig. 8 Normalized spectra in the visible wavelength range, collected at a distance of 0.1 mm from the steel and phenolic model surfaces.

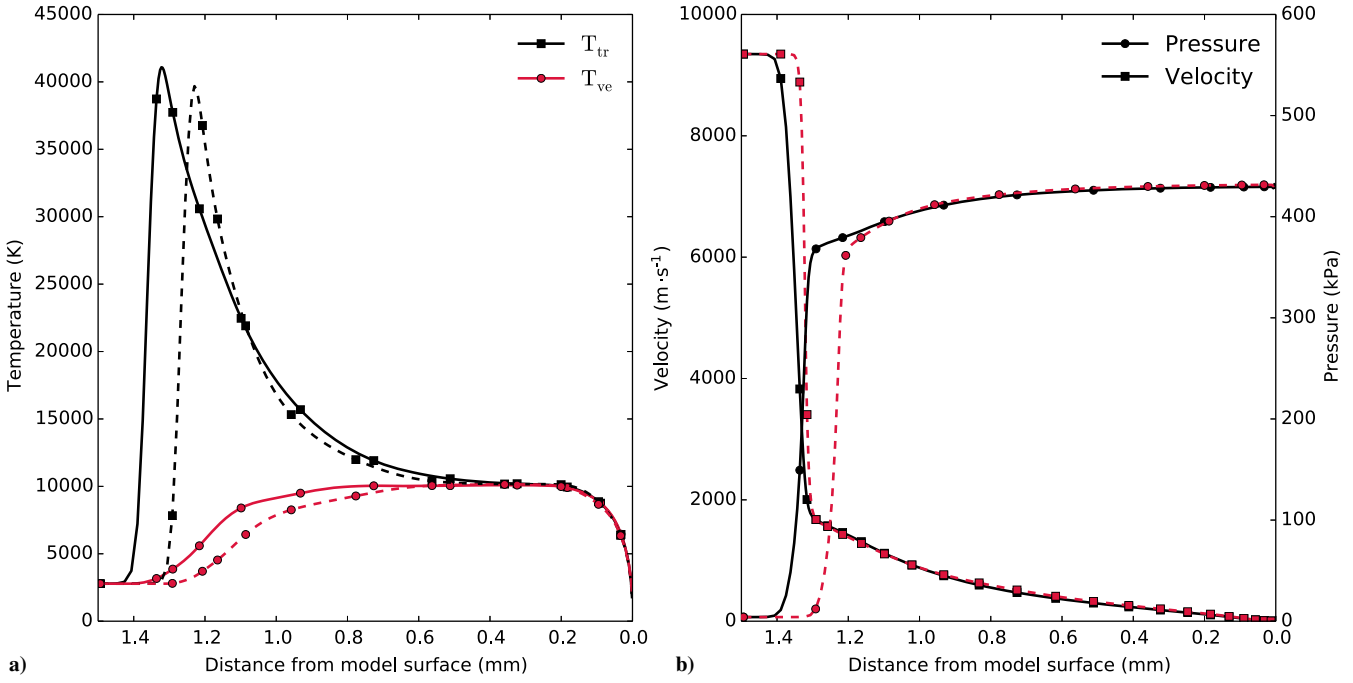

Fig. 9 Stagnation line flow profiles using the Park (solid lines) and Johnston models (dashed lines) for a) temperature and b) pressure and velocity.

equilibrate approximately 0.35 mm from the model wall at the same temperature as that obtained using the Park model. The effect of the finite-rate surface chemistry models on these temperature profiles is negligible. The stagnation pressure is higher at 432 kPa using the Johnston model, as compared with 429 kPa using the Park model (Fig. 9b).

The shock detachment distance provides a good point of comparison between the simulation and the experiment. Using the Park model, this distance was calculated to be approximately 1.4 mm, whereas a decreased distance of 1.2 mm was observed using the Johnston model. The shock detachment distance was inversely proportional to the density ratio across the shock for hypersonic blunt bodies [40]. The Johnston model, which provided higher probabilities for third-body and neutral exchange reactions involving CO and CN in particular [25], resulted in a higher post-shock density as compared to the Park model. This was the reason for the smaller shock detachment distance. Compared to the experimentally measured shock detachment distance of 1.9 mm (Fig. 6b), the Park and Johnston reaction schemes underestimated this value by 28 and 58%, respectively.

The stagnation-line species number densities are displayed in Fig. 10. For both models, the majority of species attained chemical quasi-equilibrium at a distance of 0.6 mm from the wall, which was further out from the zone where thermal equilibrium was achieved. Although a smaller shock thickness was calculated using the Johnston model, the species relaxed more rapidly to their equilibrium values. CO_2 and CO did not attain equilibrium and experienced continuous dissociation until the boundary layer, where an increase in concentration of these two species along with CN, O_2, and NO was observed, likely due to recombination. Using the Johnston model, increased dissociation was observed for CO_2 and CO, which was to be expected given the higher dissociation rates as compared to those provided in the Park model. This, in turn, led to an increase in the concentration of CN and C_2 in the shock layer.

In the boundary layer, higher recombination was observed using Johnston rates, where O_2, N_2, and NO (Fig. 10a) had higher concentrations than their Park counterparts; conversely, C, N, and O, as well as CN and C_2 (Fig. 10b), showed lower concentrations than values calculated using the Park model. Significantly higher electron density and CO^+ concentration in the shock layer is seen in Fig. 10c

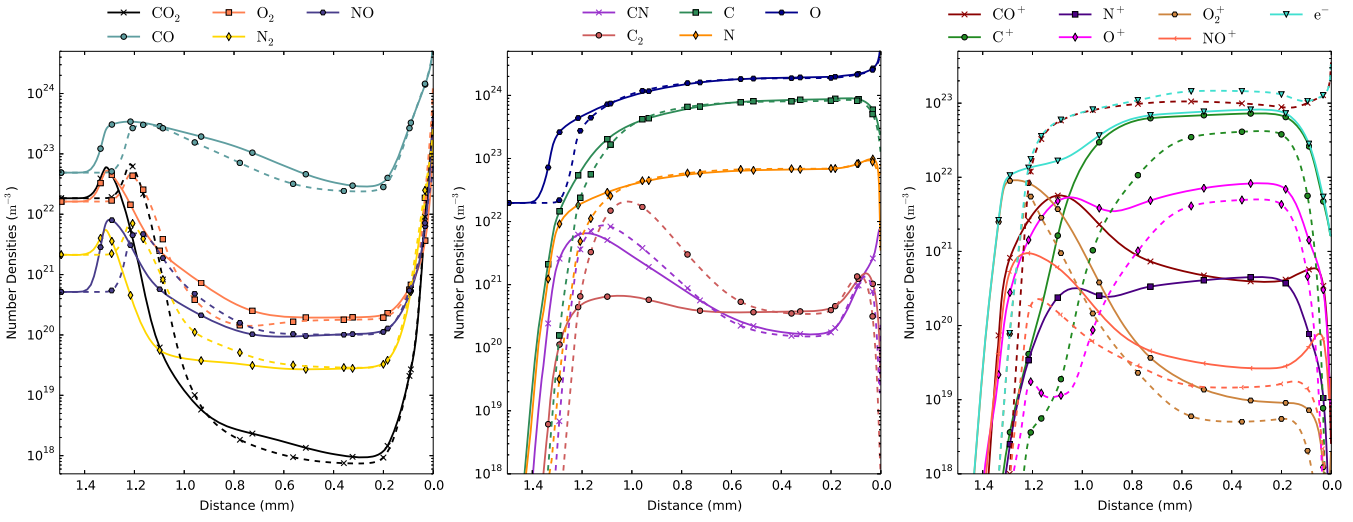

Fig. 10 Stagnation line species number density profiles using the Park (solid lines) and Johnston models (dashed lines).

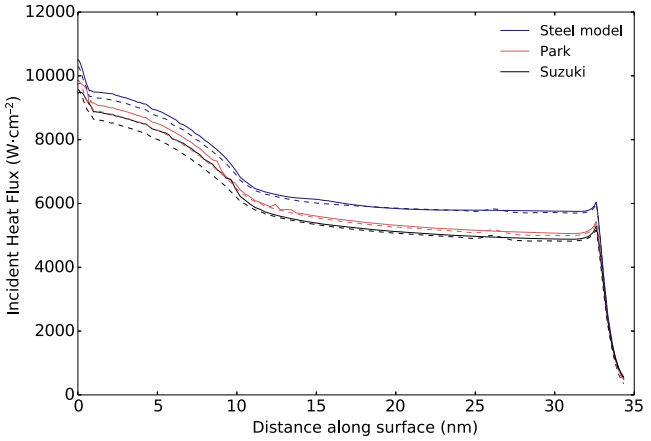

Fig. 11 Surface convective heat flux using Park (solid) and Johnston's (dashed) reactions.

using Johnston rates. This scheme omits N^+ and ion-exchange reactions, and it contains fewer electron-impact ionization and charge exchange reactions.

The convective heat flux incident on the model wall is presented in Fig. 11, which is depicted from the stagnation point to the shoulder following the contours of the aeroshell. A comparison is made between the effect of the surface kinetic rates proposed by Park [33] and by Suzuki [35], along with the underlying comparison between the Park and Johnston reaction schemes for CO_2–N_2 gas mixtures. First of all, it can be seen that, from the stagnation point to the shoulder, a lower incident convective heat flux is calculated for the cases with surface reactions as compared to the noncatalytic case. This phenomenon can be attributed to convective blockage, which is an expected result of surface reactions. The largest difference is calculated near the model shoulder (12.8% decrease, as compared to 3.5% at the stagnation point) where the lower temperature and gradients are seemingly conducive to increased production of CN and CO. The lowest heat flux value is associated with Suzuki's reduced reaction efficiency [35], as compared to the one provided the Park model. Interestingly, heat fluxes associated with the Johnston model differed significantly from the Park model, mainly around the stagnation point, in the region of highest temperatures and gradients. Near the shoulder, both models equilibrated to similar heat flux values. Compared to the heat flux incident on a nonreacting wall of 7900 $W \cdot cm^{-2}$, calculated in Sec. II.B using Sutton and Graves's empirical correlation [19], the CFD-computed stagnation-point heat flux differed by 21% using the Park model and 18% using the Johnston model.

C. Comparing CFD and Experiment

The measured absolute spectral intensities in the ultraviolet as compared with numerical spectra calculated using the `NEQAIR` code are presented in Fig. 12. The x-axis has been truncated (removing 391–410 nm) to remove contaminant lines from the aluminum and steel diaphragms for clarity. The experimental spectra were measured 0.1 mm upstream of the stagnation point, and numerical spectra were calculated at an equivalent distance from CFD solutions using both aforementioned reaction schemes. Spectra calculated with `NEQAIR` were chosen because they best matched the experimental results, whereas `PARADE` and `Photaura` overestimated all peak intensities present. A possible reason for this overestimation is that both `PARADE` [41] and `Photaura` [9] were developed and validated for Mars and Titan entry conditions, which generally occur at lower densities and velocities when compared to Venus entry. A truncated x axis is presented in Fig. 12 to remove all the Al lines, along with several Fe peaks, which otherwise serve only to clutter the plot. No other visible lines of interest were lost in this truncation.

Using the Park model, good correlation is seen for the C_2 Swan bands (Fig. 12), matching peak intensities and line widths. However, spectral radiance was substantially overestimated for the CN violet $\nu = 0$ band. This was most likely due to significant CN violet self-absorption, which was noted in a past study by Boubert and Rond [42], and it was not accounted for by any of the radiation codes considered. This overestimation was slightly reduced when the Johnston model was applied, but it was still significant. With the Johnston model, CN violet $\nu = +1$ peak intensities were better matched than with the Park model; however, all C_2 Swan band peaks were severely overestimated due to the increase in concentration along the line of sight. Both the implemented reaction schemes excluded N_2^+ due to Park et al.'s [22] hypothesis that its concentration and effect on the rate processes was insignificant. Given its intensity was of a similar order of magnitude to that of the CN violet band, its inclusion in numerical models for CO_2–N_2 flows in X2 is recommended.

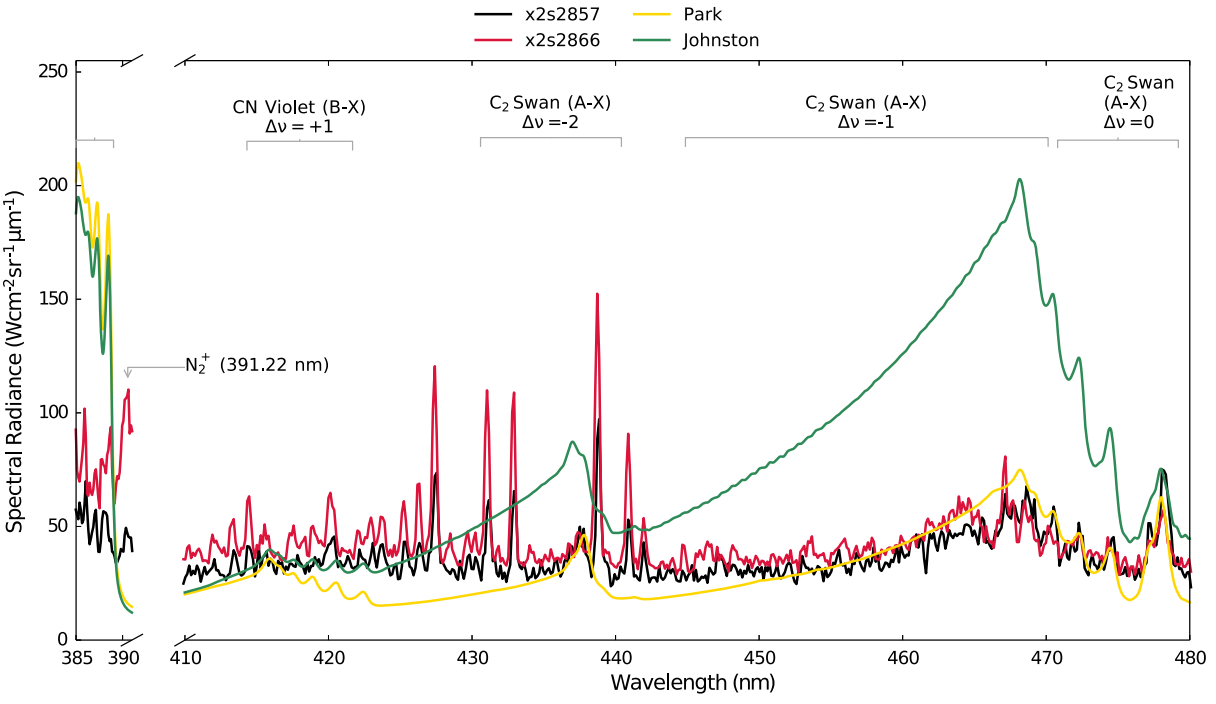

Fig. 12 Comparison of experimental UV spectra with numerical spectra calculated using NEQAIR.

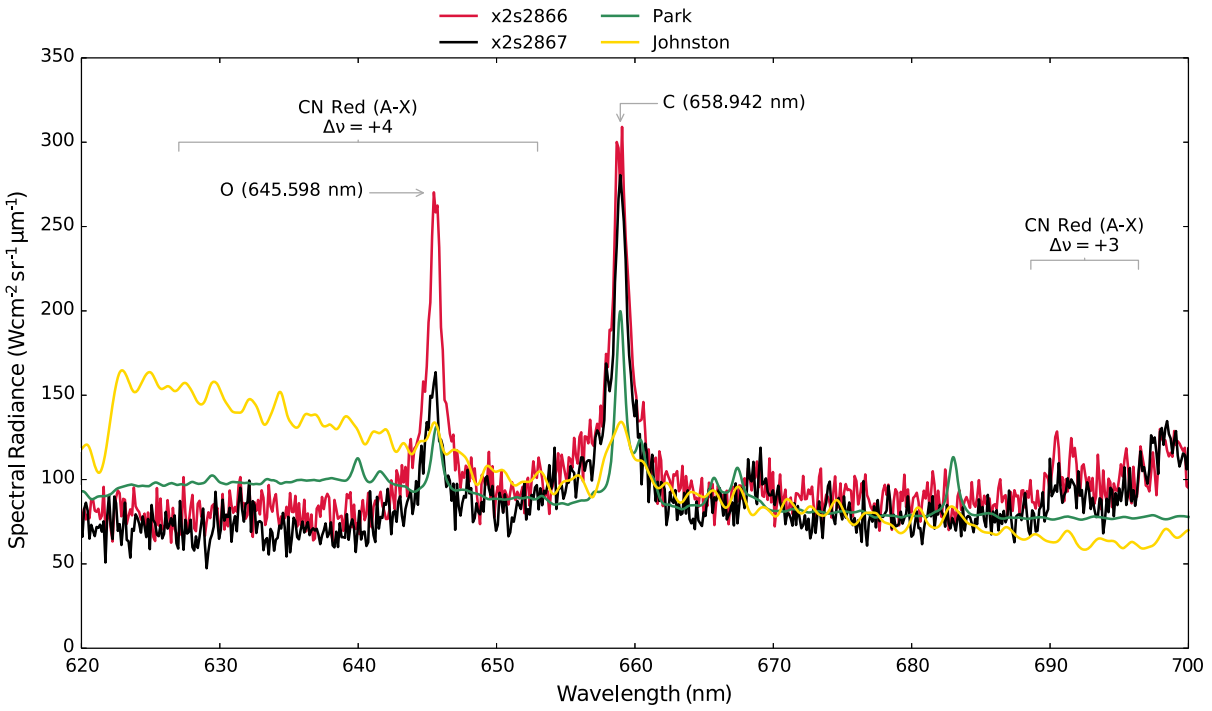

Fig. 13 Comparison of experimental visible spectra with numerical spectra calculated using NEQAIR.

Experimental spectra from the boundary layer around the composite and the steel models, measured in the visible wavelength range, as compared to numerical spectra calculated using the PARADE code are presented in Fig. 13. The Photaura and NEQAIR codes were not presented due to severe underestimation of spectral radiances at these wavelengths. The most intense lines identified were an O atomic line at 645.598 nm and a C atomic line at 658.94 nm. Several weak CN red bands were also present [43].

The comparison between experimental and numerical spectra was inconclusive for visible wavelengths, with the latter underestimating peak intensities across the entire range studied. Further work is required to understand the reasons behind this discrepancy and whether it is due to the calculated temperature in the boundary layer, the reaction or energy exchange models selected, or the radiation codes underestimating the radiative coefficients for the species involved. Use of both the Park and Suzuki finite-rate surface kinetic models had no significant effect on the generated spectra, which closely resembled the nonablating case.

The significantly higher level of background radiation and noise in the experimental spectra is an inherent disadvantage of measuring radiation in the visible wavelength range because contamination from extraneous light sources is present. The numerical spectra calculated using the Park reaction scheme were therefore shifted up to account for this background radiation. In addition to this, the radiation codes did not seem to sufficiently model the extra broadening in the spectral line wings, which have been attributed to additional contributions from neutral bremmstrahlung by Cruden et al. [44]. Spectra calculated using the Johnston model had a much higher average intensity, matching the background radiation for much of the studied range, overestimating radiance below 640 nm, and underestimating it above 690 nm. To reduce the effect of noise, Boubert and Rond [42] suggested the use of a 70% CO_2–30% N_2 gas mixture, which significantly improved the emission signal-to-noise ratio while keeping the chemical kinetic processes the same as a standard Martian or Venusian atmosphere.

V. Conclusions

A carbon–phenolic aeroshell model with electrical preheating capability was successfully designed and manufactured for use in experiments in X2 expansion tube. The chosen model shape represented a move away from those previously used for ablation testing in X2 and was more representative of entry capsule geometries. The success of applying the preheating technique was limited by the brittleness of the phenolic resin, causing it to crack and disperse at the surface. The model was therefore shock heated by the expansion tube flow to simulate surface decomposition in a Venus entry condition with a flight equivalent velocity of 9.35km $\cdot$ s^{-1}. Emission spectroscopy was used to measure radiation emitted by species in the boundary layer. As ablation studies in high-enthalpy CO_2–N_2 conditions are rare, a unique radiation dataset is presented here.

To augment the scarce set of computational aerothermodynamic simulations of Venus entry available in literature, axisymmetric 2-D computational fluid dynamic calculations were used to simulate the hypersonic nonequilibrium flowfield around the aeroshell model. The solutions were coupled to NEQAIR and PARADE radiation codes to calculate spectral radiance along the experimental line of sight, allowing a comparison with measured data for model validation. This comparison showed the presence of all the same relevant lines and good approximation of the line shape. Peak intensities in the visible wavelength range were underestimated by all models. CN violet band intensities in the ultraviolet were heavily overestimated. These bands were thought to be self-absorbed in the experiment: a phenomenon that is not accounted for by the radiation models. Excellent comparison was found between the simulated and measured spectra; in particular, the C_2 Swan band intensities using the Park chemistry model were well represented.

Acknowledgments

This work has been financially supported by the Swiss National Science Foundation (SNSF) under contract no. 200021–146710 and the SNSF Mobility scheme. All operating costs in the laboratory were funded by grants from the Australian Research Council. The authors would like to acknowledge École Polytechnique Fédérale de Lausanne's support through the use of the facilities of its Scientific Information Technology and Application Support Center. Thanks also to X2 operators and workshop staff, to Phil Teakle for providing the materials and expertise required to manufacture the models, to Dave Buttsworth for providing the integrating sphere calibration source, to the NASA Ames Research Center for NEQAIR, to the ESA for PARADE, and to Peter Jacobs and Rowan Gollan for their advice and assistance with Eilmer3.

References

[1] Bouilly, J. M., Bonnefond, F., Dariol, L., Jullien, P., and Leleu, F., "Ablative Thermal Protections for Atmospheric Entry. An Overview of Past Missions and Needs for Future Programmes," *Proceedings of the 5th European Workshop on Thermal Protection Systems and Hot Structures* [CD-ROM], edited by K. Fletcher, ESTEC European Space Agency SP-631, Noordwijk, The Netherlands, May 2006; also edited by Fletcher, K., European Space Agency ESA SP-631, 2006.

[2] Laub, B., and Venkatapathy, E., "Thermal Protection System Technology and Facility Needs for Demanding Future Planetary Missions," *Proceedings of the International Workshop Planetary Probe Atmospheric Entry and Descent Trajectory Analysis and Science*, edited by A. Wilson, ESA Publ. Div. ESA SP-544, Noordwijk, The Netherlands, 2004, pp. 239–247.

[3] Morgan, R. G., "Radiation Measurements in Simulated Ablation Layers," U.S. Air Force Office of Scientific Research TR FA23860914144, 2010.

[4] Fahy, E. J., "Superorbital Re-Entry Shock Layers: Flight and Laboratory Comparisons," Ph.D. Thesis, Univ. of Queensland, Brisbane, QLD, Australia, 2011.

[5] Buttsworth, D. R., D'Souza, M., Potter, D., Eichmann, T., Mudford, N., McGilvray, M., McIntyre, T. J., Jacobs, P. A., and Morgan, R. G., "Expansion Tunnel Radiation Experiments to Support Hayabusa Re-Entry Observations," *48th AIAA Aerospace Sciences Meeting*, AIAA Paper 2010-0634, 2010.

[6] Zander, F., Morgan, R. G., Sheikh, U., Buttsworth, D. R., and Teakle, P. R., "Hot-Wall Reentry Testing in Hypersonic Impulse Facilities," *AIAA Journal*, Vol. 51, No. 2, 2013, pp. 476–484. doi:10.2514/1.J051867

[7] Lewis, S. W., Morgan, R. G., McIntyre, T. J., Alba, C. R., and Greendyke, R. B., "Expansion Tunnel Experiments of Earth Reentry Flow with Surface Ablation," *Journal of Spacecraft and Rockets*, Vol. 53, No. 5, 2016, pp. 887–899.

[8] Gildfind, D. E., Morgan, R. G., and Jacobs, P. A., "Expansion Tubes in Australia," *Experimental Methods of Shock Wave Research*, Springer, New York, 2016, pp. 399–431.

[9] Potter, D., "Modelling of Radiating Shock Layers for Atmospheric Entry at Earth and Mars," Ph.D. Thesis, Univ. of Queensland, Brisbane, QLD, Australia, 2011.

[10] Fahy, E. J., Gollan, R. J., Buttsworth, D., Jacobs, P. A., and Morgan, R. G., "Expansion Tube and Computational Fluid Dynamics Studies of Superorbital Earth Re-Entry," *46th AIAA Thermophysics Conference*, AIAA Paper 2016-3532, 2016.

[11] Palmer, G., Prabhu, D., Brandis, A., and McIntyre, T. J., "Numerical Simulation of Radiation Measurements Taken in the X2 Facility for Mars and Titan Gas Mixtures," *42nd AIAA Thermophysics Conference*, AIAA Paper 2011-3768, 2011, p. 12.

[12] Alba, C. R., Greendyke, R. B., Lewis, S. W., Morgan, R. G., and McIntyre, T. J., "Numerical Modeling of Earth Reentry Flow with Surface Ablation," *Journal of Spacecraft and Rockets*, Vol. 53, No. 1, 2016, pp. 84–97. doi:10.2514/1.A33266

[13] Van den Berg, M., Falkner, P., Atzei, A., Phipps, A., Underwood, J., Lingard, J., Moorhouse, J., Kraft, S., and Peacock, A., "Venus Entry Probe Technology Reference Study," *Advances in Space Research*, Vol. 38, No. 11, 2006, pp. 2626–2632. doi:10.1016/j.asr.2006.03.020

[14] de Crombrugghe de Looringhe, G. A., "On Binary Scaling and Ground-to-Flight Extrapolation in High-Enthalpy Facilities," Ph.D. Thesis, University of Queensland, St. Lucia, QLD, Australia, 2017.

[15] James, C. M., Gildfind, D. E., Morgan, R. G., Lewis, S. W., Fahy, E. J., and McIntyre, T. J., "On the Current Limits of Simulating Gas Giant Entry Flows in an Expansion Tube," *20th AIAA International Space Planes and Hypersonic Systems and Technologies Conference*, AIAA Paper 2015-3501, 2015.

[16] "Cellobond™ Resin J2027L," Online Technical Data Sheet, Hexion, Columbus, OH, http://www.hexion.com/products/technicaldatasheet.aspx?id=30503 [retrieved 20 April 2017].

[17] "Torayca® T700S Data Sheet," Toray Carbon Fibers America Data Sheet CFA-005, Santa Ana, CA, http://www.toraycfa.com/pdfs/T700SDataSheet.pdf [retrieved 20 April 2017].

[18] Kraetzig, B., Buttsworth, D. R., Zander, F., and Löhle, S., "Temperature and Heat Flux Measurement on Hot Models in Short-Duration Facilities," *Journal of Thermophysics and Heat Transfer*, Vol. 29, No. 1, 2015, pp. 37–46. doi:10.2514/1.T4309

[19] Sutton, K., and Graves, R. A., Jr., "A General Stagnation-Point Convective Heating Equation for Arbitrary Gas Mixtures," NASA TR-R-376, 1971.

[20] Rivell, T., "Notes on Earth Atmospheric Entry for Mars Sample Return Missions," NASA TP-2006-213486, 2006.

[21] Gollan, R. J., and Jacobs, P. A., "About the Formulation, Verification and Validation of the Hypersonic Flow Solver Eilmer," *International Journal for Numerical Methods in Fluids*, Vol. 73, No. 1, 2013, pp. 19–57. doi:10.1002/fld.v73.1

[22] Park, C., Howe, J. T., Jaffe, R. L., and Candler, G. V., "Review of Chemical-Kinetic Problems of Future NASA Missions. II—Mars Entries," *Journal of Thermophysics and Heat Transfer*, Vol. 8, No. 1, 1994, pp. 9–23. doi:10.2514/3.496

[23] Park, C., and Ahn, H. K., "Stagnation-Point Heat Transfer Rates for Pioneer-Venus Probes," *Journal of Thermophysics and Heat Transfer*, Vol. 13, No. 1, 1999, pp. 33–41. doi:10.2514/2.6426

[24] Treanor, C. E., and Marrone, P. V., "Effect of Dissociation on the Rate of Vibrational Relaxation," *Physics of Fluids (1958–1988)*, Vol. 5, No. 9, 1962, pp. 1022–1026. doi:10.1063/1.1724467

[25] Johnston, C. O., and Brandis, A. M., "Modeling of Nonequilibrium CO Fourth-Positive and CN Violet Emission in CO_2–N_2 Gases," *Journal of Quantitative Spectroscopy and Radiative Transfer*, Vol. 149, Dec. 2014, pp. 303–317. doi:10.1016/j.jqsrt.2014.08.025

[26] Palmer, G. E., and Wright, M. J., "Comparison of Methods to Compute High-Temperature Gas Viscosity," *Journal of Thermophysics and Heat Transfer*, Vol. 17, No. 2, 2003, pp. 232–239. doi:10.2514/2.6756

[27] Palmer, G. E., and Wright, M. J., "A Comparison of Methods to Compute High Temperature Gas Thermal Conductivity," AIAA Paper 2003-3913, 2003.

[28] Laricchiuta, A., Bruno, D., Capitelli, M., Catalfamo, C., Celiberto, R., Colonna, G., Diomede, P., Giordano, D., Gorse, C., and Longo, S., Pagano, D., and Pirani, F., "High Temperature Mars Atmosphere. Part I: Transport Cross Sections," *European Physical Journal D*, Vol. 54, No. 3, 2009, pp. 607–612. doi:10.1140/epjd/e2009-00192-7

[29] Wright, M. J., Hwang, H. H., and Schwenke, D. W., "Recommended Collision Integrals for Transport Property Computations Part II: Mars and Venus Entries," *AIAA Journal*, Vol. 45, No. 1, 2007, pp. 281–288. doi:10.2514/1.24523

[30] Ramshaw, J. D., and Chang, C. H., "Ambipolar Diffusion in Two-Temperature Multicomponent Plasmas," *Plasma Chemistry and Plasma Processing*, Vol. 13, No. 3, 1993, pp. 489–498. doi:10.1007/BF01465878

[31] Roache, P. J., "Quantification of Uncertainty in Computational Fluid Dynamics," *Annual Review of Fluid Mechanics*, Vol. 29, No. 1, 1997, pp. 123–160.

[32] "Editorial Policy Statement on Numerical Accuracy and Experimental Uncertainty," *AIAA Journal*, Vol. 31, No. 1, 1994, pp. 3–3.

[33] Park, C., Jaffe, R. L., and Partridge, H., "Chemical-Kinetic Parameters of Hyperbolic Earth Entry," *Journal of Thermophysics and Heat Transfer*, Vol. 15, No. 1, 2001, pp. 76–90. doi:10.2514/2.6582

[34] Candler, G. V., "Nonequilibrium Processes in Hypervelocity Flows: An Analysis of Carbon Ablation Models," *50th AIAA Aerospace Sciences Meeting*, AIAA Paper 2012-0724, 2012.

[35] Suzuki, T., Fujita, K., and Sakai, T., "Graphite Nitridation in Lower Surface Temperature Regime," *Journal of Thermophysics and Heat Transfer*, Vol. 24, No. 1, 2010, pp. 212–215. doi:10.2514/1.43265

[36] Smith, A., Beck, J., Fertig, M., Liebhart, H., and Marraffa, L., "Plasma Radiation Database PARADE V3. 1," European Space Agency TR28/96, Vol. 8, ESTEC, Noordwijk, The Netherlands, 2011.

[37] Brandis, A. M., Johnston, C. O., Cruden, B. A., Prabhu, D., and Bose, D., "Validation of High Speed Earth Atmospheric Entry Radiative Heating from 9.5 to 15.5 km/s," AIAA Paper 2012-2865, 2012.

[38] Palmer, G., Allen, G., Tang, C., and Brown, J., "Coupled Fluids-Radiation Analysis of a High-Mass Mars Entry Vehicle," AIAA Paper 2011-3495, 2011.

[39] Eichmann, T. N., "Radiation Measurements in a Simulated Mars Atmosphere," Ph.D. Thesis, Univ. of Queensland, Brisbane, QLD, Australia, 2012.

[40] Anderson, J. D., *Hypersonic and High Temperature Gas Dynamics*, AIAA, Reston, VA, 2000, p. 611.

[41] Joiner, N., Beck, J., Capitelli, M., Fertig, M., Herdrich, G., Laricchiuta, A., Liebhart, H., da Silva, M. L., Marraffa, L., Reynier, P., and Tran, P., "Validation of Aerothermal Chemistry Models for Re-Entry Applications: Theoretical and Computational Synthesis," *8th European Symposium on Aerothermodynamics for Space Vehicles*, European Space Agency, Noordwijk, The Netherlands, 2015.

[42] Boubert, P., and Rond, C., "Nonequilibrium Radiation in Shocked Martian Mixtures," *Journal of Thermophysics and Heat Transfer*, Vol. 24, No. 1, 2010, pp. 40–49. doi:10.2514/1.45385

[43] Bogdanoff, D. W., "Shock Tube Experiments for Earth and Mars Entry Conditions," NATO TR RTO-EN-AVT-162, Brussels, Belgium, 2009.

[44] Cruden, B. A., Martinez, R., Grinstead, J. H., and Olejniczak, J., "Simultaneous Vacuum Ultraviolet Through Near IR Absolute Radiation Measurement with Spatiotemporal Resolution in an Electric Arc Shock Tube," *41st AIAA Thermophysics Conference*, AIAA Paper 2009-4240, 2009.